Nanoscale magnetic biotransport with application to magnetofection

E. P. Furlani* and K. C. Ng
Institute for Lasers, Photonics and Biophotonics, State University of New York at Buffalo, Buffalo, New York, 14260, USA
(Received 26 February 2008; revised manuscript received 25 March 2008; published 17 June 2008)

We present a model for predicting the transport of biofunctional magnetic nanoparticles in a passive magnetophoretic system that consists of a fluidic chamber positioned above a rare-earth magnet. The model is based on a drift-diffusion equation that governs the particle concentration in the chamber. We solve this equation numerically using the finite volume method. We apply the model to the magnetofection process wherein the magnetic force produced by the magnet attracts magnetic carrier particles with surface-bound gene vectors toward the bottom of the chamber for transfection with target cells. We study particle transport and accumulation as a function of key variables. Our analysis indicates that the particles are magnetically focused toward the center of the chamber during transport, and that the rate of accumulation at the base can be enhanced using larger particles and/or by reducing the spacing between the magnet and the chamber. The model provides insight into the physics of particle transport at the nanoscale and enables rapid parametric analysis of particle accumulation, which is useful for optimizing novel magnetofection systems.

DOI: 10.1103/PhysRevE.77.061914 PACS number(s): 87.10.−e, 87.80.Fe, 87.85.Tu, 87.85.Rs

I. INTRODUCTION

Magnetic nanoparticles are finding increasing use in bioapplications, primarily as carrier particles for biomaterials such as cells, proteins, antigens, and DNA [1–5]. The use of biofunctional magnetic particles enables selective manipulation and immobilization of a biomaterial using an applied magnetic field. Furthermore, magnetic transport of such particles enables accelerated delivery of a biomaterial to a target tissue, thereby overcoming diffusion-limited accumulation. This is useful for applications such as magnetofection wherein carrier particles with surface-bound gene vectors are magnetically attracted toward target cells for transfection [6–14]. In a typical *in vitro* magnetofection system, target cells are located at the bottom of a fluidic chamber (well of a culture plate), and a rare-earth magnet beneath the chamber provides a magnetic force that attracts the biofunctional particles toward the cells as shown in Fig. 1. Magnetofection has significant advantages over traditional transfection methods [6–8]: (i) the process time is dramatically reduced, e.g., peak transfection levels can be achieved with a particle/cell incubation time on the order of 10 min, as compared to 2–4 h for standard methods; (ii) high transfection rates can be obtained with significantly lower vector doses; (iii) an increase in the gene transfer efficiency of up to five orders of magnitude can be realized; and (iv) gene delivery can be achieved with nonpermissive cells. However, despite the advantages and growing use of magnetofection, relatively few authors have studied particle transport and accumulation for this process. Nanoscale transport models are needed for the development and optimization of novel mesoscale and microscale magnetofection systems.

In this paper, we study the transport and accumulation of magnetic nanoparticles in a passive magnetophoretic system that consists of a fluidic chamber positioned above a cylindrical rare-earth magnet. We model particle transport using a drift-diffusion equation that governs the particle concentration within the chamber. This equation takes into account Brownian motion as well as the fluidic, magnetic, and gravitational forces on the particles. We obtain an analytical expression for the magnetic force, which simplifies the transport analysis. We solve the drift-diffusion equation numerically using the finite volume method (FVM), and apply boundary conditions that mimic the magnetofection process. We use the model to study particle transport as a function of key variables using both one-dimensional (1D) and 2D analysis. Our analysis indicates that the magnetic force focuses the particles toward the center of the chamber during transport, and that the rate of particle accumulation at the base of chamber can be controlled by choosing different sized particles and/or by adjusting the spacing between the magnet and the chamber. The model provides insight into the physics of particle transport and is useful for optimizing the performance of novel magnetofection systems.

II. THEORY

A. Equation of motion

The motion of a magnetic particle in a fluid under the influence of an applied field is governed by several forces including (a) the magnetic force, (b) fluidic drag, (c) particle/fluid interactions (perturbations to the flow field), (d) buoyancy, (e) thermal kinetics, and (f) interparticle effects such as magnetic dipole interactions [15,16]. We consider the behavior of nanoparticles in low concentration and neglect particle/fluid interactions and interparticle effects. We model the transport of the nanoparticles using a drift-diffusion equation for the particle volume concentration $c(t)$ [17–22],

$$\frac{\partial c}{\partial t} = \nabla \cdot (D \nabla c - \mathbf{U}c), \tag{1}$$

where $D=\mu kT$, η is the fluid viscosity (Stokes' approximation), and $\mu=1/(6\pi\eta R_{p,\mathrm{hyd}})$ is the mobility of a particle with

*Author to whom all correspondence should be addressed. efurlani@buffalo.edu

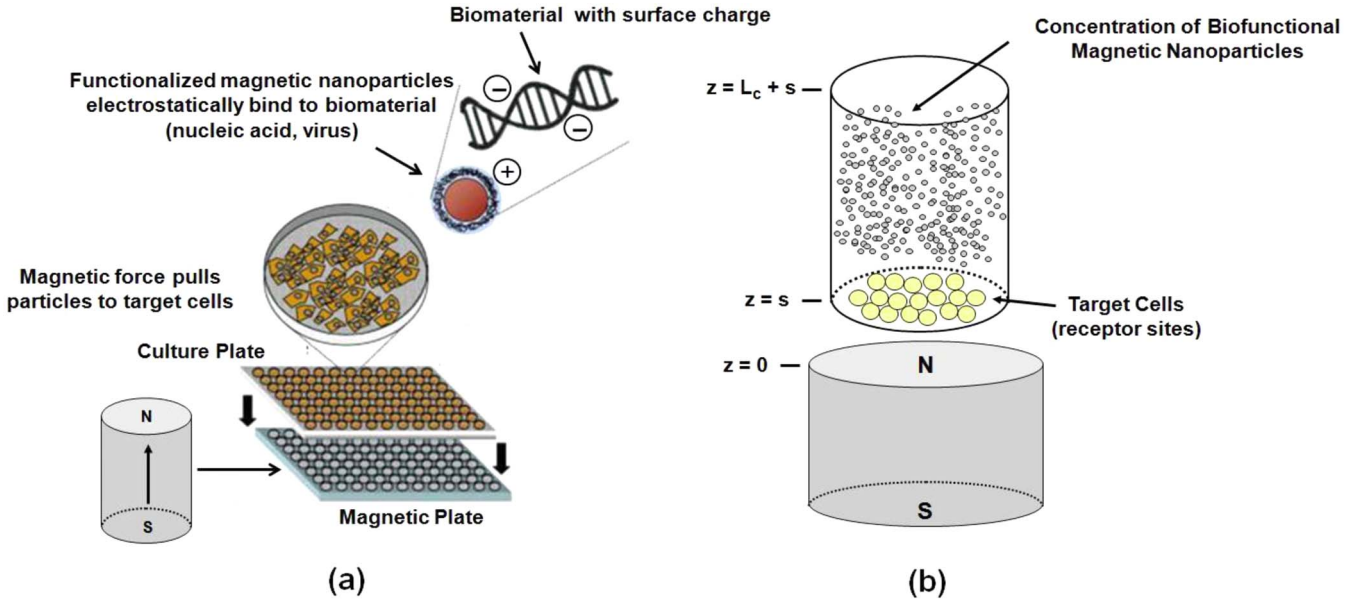

FIG. 1. (Color online) Magnetofection: (a) array of cell cultures positioned above an array of cylindrical rare-earth magnets (adapted from [6]), (b) the magnetic force pulls magnetic nanoparticles with surface bound gene vectors toward the cells.

an effective hydrodynamic radius $R_{p,\mathrm{hyd}}$, which takes into account surface-bound biomaterial. $\mathbf{U}=\mu\mathbf{F}$ is the drift velocity and $\mathbf{F}$ is the total force on the particle. In our analysis, we take into account the fluidic $\mathbf{F}_f$, magnetic $\mathbf{F}_m$, and gravitational (buoyancy) $\mathbf{F}_g$ forces. The fluidic force is based on Stokes' approximation for the drag on a sphere in a viscous fluid, i.e.,

$$\mathbf{F}_f = -6\pi\eta R_{p,\mathrm{hyd}}(\mathbf{v}_p - \mathbf{v}_f), \tag{2}$$

where $\mathbf{v}_p$ and $\mathbf{v}_f$ are the particle and fluid velocity, respectively. The drift velocity is obtained in the limit of negligible particle inertia $[m_p(dv_p/dt)\rightarrow 0]$, i.e., by setting

$$\mathbf{F}_m + \mathbf{F}_f + \mathbf{F}_g = 0. \tag{3}$$

We substitute $\mathbf{v}_p=\mathbf{U}$ into Eq. (3) and obtain $\mathbf{U}=\mu(6\pi\eta R_{p,\mathrm{hyd}}\mathbf{v}_f+\mathbf{F}_m+\mathbf{F}_g)$. Note that if the Stokes drag is the only force, then $\mathbf{U}=\mathbf{v}_f$. In our analysis below, we assume that the fluid is stationary, and therefore $\mathbf{U}=\mu(\mathbf{F}_m+\mathbf{F}_g)$.

B. Magnetic force

We model the magnetic force on a nanoparticle using the "effective" dipole moment method in which a magnetic particle is replaced by an "equivalent" point dipole with a moment $\mathbf{m}_{p,\mathrm{eff}}$ [23,24]. The force on the dipole (and hence on the particle) is given by

$$\mathbf{F}_m = \mu_f(\mathbf{m}_{p,\mathrm{eff}}\cdot\nabla)\mathbf{H}_a, \tag{4}$$

where μ_f is the permeability of the transport fluid, $\mathbf{m}_{p,\mathrm{eff}}$ is the "effective" dipole moment of the particle, and $\mathbf{H}_a$ is the (externally) applied magnetic-field intensity at the center of the particle, where the equivalent point dipole is located. It is important to note that $\mathbf{m}_{p,\mathrm{eff}}$ depends on $\mathbf{H}_a$. We determine $\mathbf{F}_m$ using analytical expressions for $\mathbf{m}_{p,\mathrm{eff}}$ and $\mathbf{H}_a$, which we develop below.

1. Effective dipole model

In order to determine $\mathbf{m}_{p,\mathrm{eff}}$, we need a model for the magnetization of the particles. Consider a magnetic nanoparticle with a radius R_p and volume V_p. A magnetization model that takes into account self-demagnetization and magnetic saturation has developed by Furlani [23,25–27]. In this model, $\mathbf{m}_{p,\mathrm{eff}}=V_p f(H_a)\mathbf{H}_a$, where

$$f(H_a) = \begin{cases} \dfrac{3(\chi_p-\chi_f)}{(\chi_p-\chi_f)+3} & H_a < \left(\dfrac{(\chi_p-\chi_f)+3}{3\chi_p}\right)M_{\mathrm{sp}} \\ M_{\mathbf{sp}}/H_a & H_a \geq \left(\dfrac{(\chi_p-\chi_f)+3}{3\chi_p}\right)M_{\mathrm{sp}} \end{cases} \tag{5}$$

and χ_p and χ_f are the magnetic susceptibilities of the particle and fluid, respectively, and $M_{\mathbf{sp}}$ is the saturation magnetization of the particle. Equations (4) and (5) provide a model for predicting the magnetic force on nanoparticles taking into account particle magnetization including self-demagnetization and saturation effects, i.e.,

$$\mathbf{F}_m = \mu_f V_p f(H_a)(\mathbf{H}_a\cdot\nabla)\mathbf{H}_a. \tag{6}$$

2. Magnetic field

We develop analytical expressions for the magnetic field and force distribution of a uniformly magnetized cylindrical magnet, which is commonly used in magnetofection [28]. The field problem for this geometry involves axisymmetric analysis. In this section, we obtain a 1D solution. A 2D solution is presented in the Appendix.

In the 1D approximation, the field and force are strictly in the z direction, i.e., no radial components. This approximation is reasonable when the diameter of the magnet is much greater than the diameter and height of the fluidic chamber.

The 1D (on-axis) field solution for a cylindrical rare-earth magnet that is magnetized to a saturation level M_s is well known (see p 129 in [29]),

$$H_{az}(z) = \frac{M_s}{2}\left(\frac{z+L_m}{\sqrt{(z+L_m)^2+R_m^2}} - \frac{z}{\sqrt{z^2+R_m^2}}\right), \quad (7)$$

where z is the distance above the top of the magnet, and L_m and R_m are the length and radius of the magnet, respectively. From Eqs. (6) and (7), we find that the magnetic force along the z axis above the magnet is given by

$$\mathbf{F}_{mz}(z) = \mu_0 V_p f(H_a)\frac{M_s^2 R_m^2}{4}\left(\frac{(z+L_m)}{[(z+L_m)^2+R_m^2]^2} + \frac{z}{(z^2+R_m^2)^2} - \frac{(z+L_m)[(z+L_m)^2+R_m^2]+z(z^2+R_m^2)}{(z^2+R_m^2)^{3/2}[(z+L_m)^2+R_m^2]^{3/2}}\right). \quad (8)$$

As noted above, a 2D field and force expressions are derived in the Appendix.

III. SOLUTION METHOD

We solve the drift-diffusion equation (1) numerically using the finite-volume method (FVM). The physical domain is discretized into a system of computational cells with each cell centered on a computational node. We develop both 1D and 2D models. The 1D model enables rapid parametric analysis of particle accumulation as a function of key variables and provides insight into magnetophoresis at the nanoscale. The 2D model provides a detailed understanding of the distribution of particles throughout the fluidic chamber and the accumulation of particles on its base.

In the 1D model, the FVM discretization of Eq. (1) at an interior node is

$$c_i^{n+1} = c_i^n - \frac{\delta t}{\delta z}(P_{i+1/2} - P_{i-1/2}) \quad (i = 1,2,\ldots,N_z), \quad (9)$$

where $\delta z = L_c/N_z$ is the length of a computational cell and L_c is the length of the chamber. c_i^n and c_i^{n+1} are the values of the concentration at the ith computational node at time steps n and $n+1$, respectively. $P_{i\pm 1/2}$ is a discretized version of the particle flux $-[D(\partial c/\partial z) - Uc]$ at the edges of the computational cell $z_{i\pm 1/2}$. We use an upwind scheme and obtain

$$P_{i+1/2} = -\left(D\frac{c_{i+1}^n - c_i^n}{\delta z} - [\min(U_i,0)c_i^n + \max(U_{i-1},0)c_{i-1}^n]\right). \quad (10)$$

Let $z_{c,t}$ and $z_{c,b}$ denote the locations of the top and bottom of the chamber, respectively, and let s denote the spacing between the top of the magnet and the bottom of the chamber [Fig. 1(b)]. The magnetic field solutions Eqs. (7) and (A5) apply when the top of the magnet is at $z=0$, and therefore $z_{c,t}=L_c+s$ and $z_{c,b}=s$ [Fig. 1(b)]. We solve Eq. (9) subject to an initial condition in which there is a uniform particle volume concentration throughout the chamber $c(z,0)=c_0$. We apply a zero-flux Neumann boundary condition at the top of the chamber and a Dirichlet condition $c(z_{c,b},t)=0$ at the bottom. The latter condition mimics the magnetofection process wherein nanoparticles that reach the bottom of the chamber are removed from the computation as it is assumed that they bind with receptor sites on target cells and therefore no longer influence particle transport. It is assumed that there are a sufficient number of receptors to accommodate all of the particles in the chamber. We compute particle accumulation by summing the number of particles that reach the base of the chamber during each time step.

In the 2D model, we solve Eq. (1) for $c(t)$ inside the fluidic chamber. The analysis is axisymmetric because of the symmetry of the chamber as well as the magnetic force. The drift-diffusion equation is of the form

$$\frac{\partial c}{\partial t} = \frac{1}{r}\frac{\partial}{\partial r}\left[r\left(D\frac{\partial c}{\partial r} - U_r c\right)\right] + \frac{\partial}{\partial z}\left(D\frac{\partial c}{\partial z} - U_z c\right), \quad (11)$$

where U_r and U_z are drift velocities in the r and z directions. The computational domain is $0 \le r \le R_c$ and $z_{c,b} \le z \le z_{c,t}$, where R_c is the radius of chamber and $z_{c,b}$ and $z_{c,t}$ are as above. The FVM discretization of Eq. (11) at an interior node (i,j) takes the form

$$c_{i,j}^{n+1} = c_{i,j}^n - \delta t\left(\frac{1}{r_i}\frac{r_{i+1/2}P_{i+1/2,j} - r_{i-1/2}P_{i-1/2,j}}{\delta r} + \frac{Q_{i,j+1/2} - Q_{i,j-1/2}}{\delta z}\right), \quad (12)$$

where $P_{i\pm 1/2,j}$ and $Q_{i,j\pm 1/2}$ represent the particle flux through the edges of the computational cell surrounding the node along the r and z directions, respectively. We use an upwind scheme to obtain the particle flux,

$$P_{i+1/2,j} = -\left(D\frac{c_{i+1,j}^n - c_{i,j}^n}{\delta r} - [\min(U_{r,i+1,j},0)c_{i+1,j}^n + \max(U_{r,i,j},0)c_{i,j}^n]\right) \quad (13)$$

and

$$Q_{i,j+1/2} = -\left(D\frac{c_{i,j+1}^n - c_{i,j}^n}{\delta z} - [\min(U_{z,i,j+1},0)c_{i,j+1}^n + \max(U_{z,i,j},0)c_{i,j}^n]\right). \quad (14)$$

We solve Eq. (11) with zero-flux Neumann boundary conditions imposed at the top ($z=z_{z,t}$) and outer edge ($r=R_c$) of the chamber, and a Dirichlet condition $c(r,z_{c,b},t)=0$ imposed at the base to mimic magnetofection as in the 1D case.

IV. RESULTS

We use the particle transport model to study the accumulation of magnetite (Fe_3O_4) nanoparticles in a magnetophoretic system that consists of a cylindrical fluidic chamber above a rare-earth NdFeB magnet. In our analysis, the chamber has a radius $R_c=2$ mm and length $L_c=3$ mm, and is positioned 1 mm above the magnet. The magnet has a radius $R_m=2.5$ mm and length $L_m=5$ mm and is magnetized to saturation, $M_s=8\times 10^5$ A/m ($B_r=1$ T). The chamber and

magnet dimensions are representative of a standard 96 well culture plate, which is commonly used for magnetofection. We assume that the fluid in the chamber is nonmagnetic ($\chi_f=0$) with a viscosity and density equal to that of water, $\eta=0.001$ N s/m^2, and $\rho_f=1000$ kg/m^3. Fe_3O_4 nanoparticles have a density $\rho_p=5000$ kg/m^3 and a saturation magnetization $M_{sp}=4.78\times10^5$ A/m. Throughout this section, without loss of generality, we assume that the hydrodynamic radius of the particle is the same as its physical radius $R_{p,hyd}=R_p$. We adopt a magnetization model that is consistent with Eq. (5) when $\chi_p \gg 1$, i.e. [23],

$$f(H_a)=\begin{cases} 3 & H_a < M_{sp}/3 \\ M_{sp}/H_a & H_a \geq M_{sp}/3. \end{cases} \tag{15}$$

We first study the magnetic force. We compute the force along a series of horizontal lines $0\leq r\leq 2R_m$ corresponding to different heights $z=1$, 1.5, 2, 2.5, and 3 mm above the magnet. We choose a particle radius $R_p=100$ nm and evaluate the force using Eqs. (A2) and (A3). We compare the analytical force values with corresponding numerical data obtained using finite element analysis (FEA). The COMSOL Multiphysics software was used for the FEA.

As shown in Fig. 2, the magnitude of the force varies across the chamber and decreases with distance from the magnet. The maximum force on the particle is sub-nano-Newton, but substantially greater forces can be achieved using larger particles as the force scales with R_p^3. The axial force F_{mz} attracts particles downward toward the surface of the magnet, and farther from the magnet it is strongest along the z axis (centerline of the magnet). However, closer to the magnet it peaks off-axis, which implies that the particles will have a pronounced accumulation in an annulus at the bottom of the chamber. The radial force F_{mr} peaks (in a negative sense) above the radial edge of the magnet and acts to move the particles radially inward toward the z axis, away from the edge. Thus, particle accumulation is expected to be focused toward the center of the chamber and minimal near the edge of the magnet. We examine the distribution of accumulated particles in more detail in our 2D analysis below.

Next, we perform two 1D parametric studies to understand particle accumulation as a function of particle size and magnet-to-chamber spacing, respectively. In the first study, we compute particle accumulation as a function of particle radius for $R_p=0.1-500$ nm. For each radius, we determine the time required for all of the particles to reach the bottom of the chamber; we call this the saturation time τ_{sat}. As shown in Fig. 3, our analysis indicates that there are two distinct modes of transport: diffusion-dominated transport, which applies for smaller particles ($R_p<5$ nm), and drift-dominated transport, which applies for larger particles ($R_p>5$ nm). We find that τ_{sat} increases with R_p in diffusion-dominated transport, but decreases with $1/R_p^2$ in drift-dominated transport. The first result can be understood by considering the time τ_{dif} required for a particle to diffuse a distance d, $\tau_{dif}\propto d^2/D$; it follows that $\tau_{dif}\propto R_p$. This is in contrast to drift-dominated transport wherein larger particles have a higher drift velocity. Specifically, to first order $v_p=\mu F_m$ and from Eq. (6) and the definition of the mobility it follows that $v_p\propto R_p^2$, which implies that $\tau_{sat}\propto 1/R_p^2$. Practical magnetofection systems operate in a drift-dominated mode with particle sizes that range from 100 to 1000 nm in diameter (see www.bocascientific.com and [6–8]). The accumulation rates for these systems are orders of magnitude faster than diffusion-limited accumulation [28].

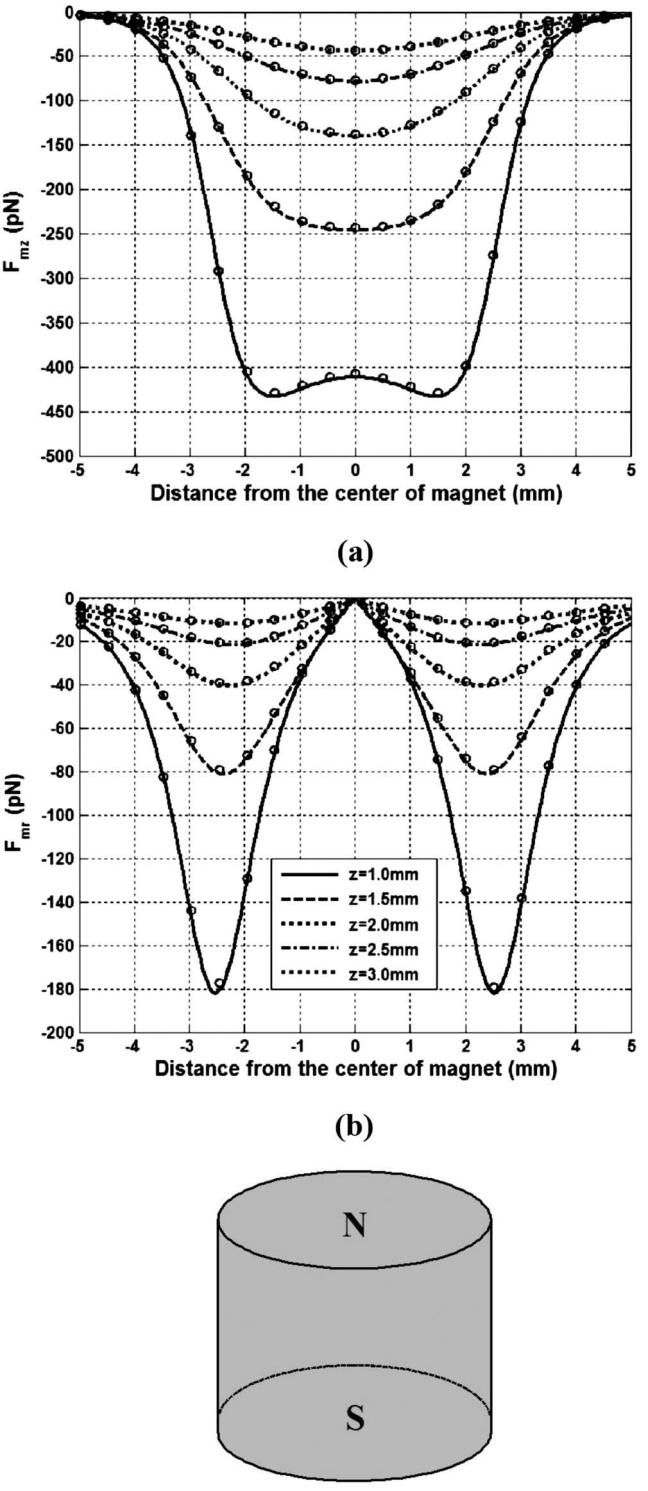

FIG. 2. Magnetic force above a cylindrical rare-earth magnet (o=FEA): (a) F_{mz}, (b) F_{mr}.

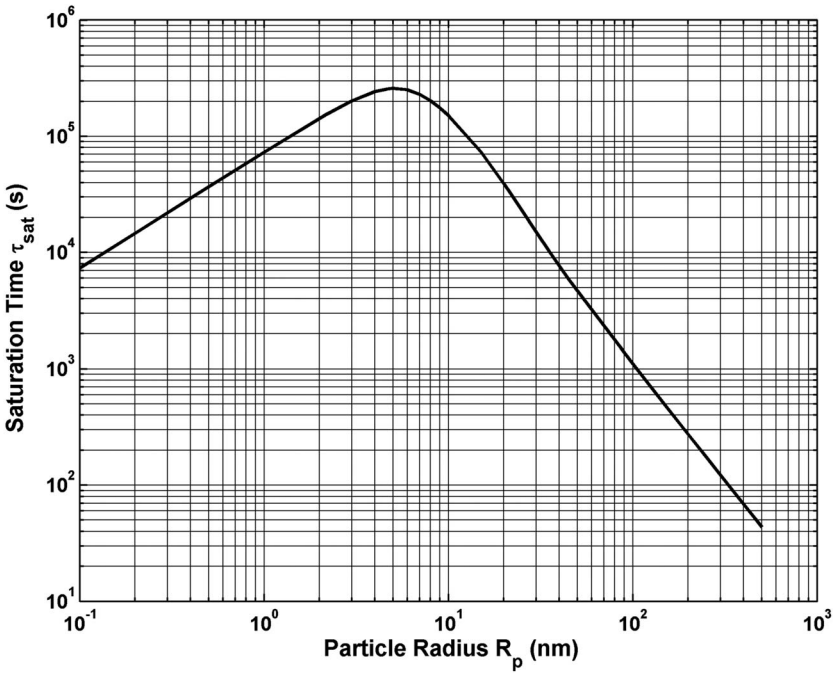

FIG. 3. Particle saturation time τ_{sat} vs particle radius R_p.

In the second 1D study, we fix the particle radius $R_p = 50$ nm and compute particle accumulation as a function of the separation s between the magnet and the chamber. From our previous analysis, we know that the transport of this particle is drift-dominated. We study particle accumulation for $s=0.5$, 1.0, 1.5, 2.0, and 2.5 mm, and we compare this with diffusion-limited accumulation, i.e., with no applied field [Fig. 4(a)]. We find that the rate of magnetically induced accumulation is orders of magnitude faster than that of diffusion-limited (no field) accumulation, which is consistent with experimental data shown in Fig. 4(b) [28]. Furthermore, the rate of accumulation increases substantially with decreasing separation.

In our last study, we perform a 2D drift-diffusion analysis to understand the distribution of accumulated particles at the base of the chamber. All dimensions are as above and the chamber is positioned 1 mm above the magnet. We compute the accumulation of particles with a radius $R_p = 100$ nm. The radial distribution of accumulated particles represented in terms of the particle volume concentration per unit area at the base of the chamber is shown in Fig. 5. Note that a higher concentration of particles occurs near the z axis (centerline) above the magnet. This is due to the magnetic focusing of the particles during transport. There is also a local maximum in the concentration in an annulus around the centerline, which is due to the off-axis peaks in the axial force F_{mz} near the magnet as shown in Fig. 2(b). We also compute the total particle accumulation at the base of the chamber as a function of the radial distance r from the center of the chamber. We integrate the particle number density n, which is obtained from the concentration c using the relation $n = c/V_p$. A normalized plot of the particle accumulation is shown in Fig. 6. Note that the majority of the particles accumulate toward the center of the chamber away from the edge of the magnet, where they are repelled inward by the magnetic force. This implies that higher transfection efficiencies will be achieved when the fluidic chamber has a smaller radius than the magnet.

V. CONCLUSIONS

We have developed a model for predicting the transport and accumulation of biofunctional magnetic nanoparticles that are confined to a fluidic chamber above a rare-earth magnet. The model involves the solution of 1D and 2D drift-diffusion equations that govern the particle concentration in the chamber. We have solved these equations subject to boundary conditions that mimic the magnetofection process. We have used the model to study particle accumulation at the base of the chamber as a function of particle size and magnet-to-chamber spacing. Our analysis indicates that particles need to be sufficiently large (tens of nanometers) to enable drift-dominated transport, and that the accumulation is greater toward the center of the chamber away from the edge of the magnet. For drift-dominated transport, the rate of accumulation increases with the particle radius, and is inversely proportional to the magnet-to-chamber separation. We have found that magnetically induced particle transport enables accumulation that is orders of magnitude faster than diffusion-limited accumulation, which is consistent with experimental observations. The model presented here provides a fundamental understanding of magnetophoresis at the nanoscale and enables the optimization of novel magnetofection systems.

APPENDIX

In this appendix, we obtain a 2D analytical expression for the magnetic force of the cylindrical permanent magnet

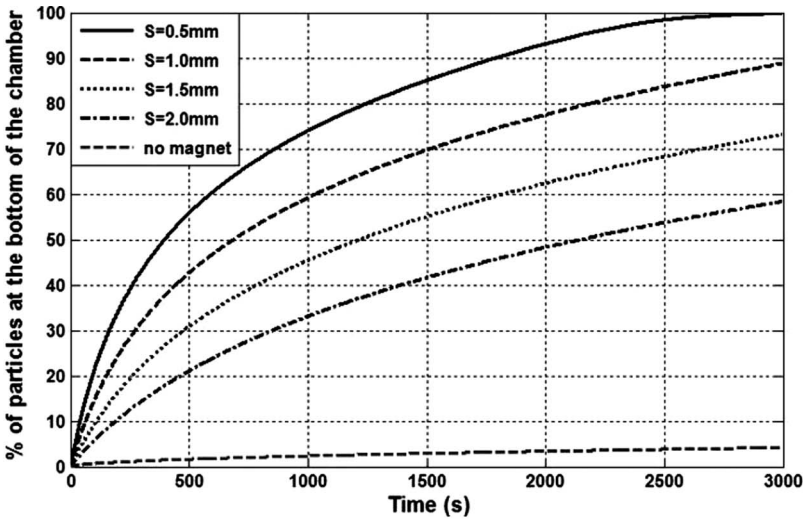

(a)

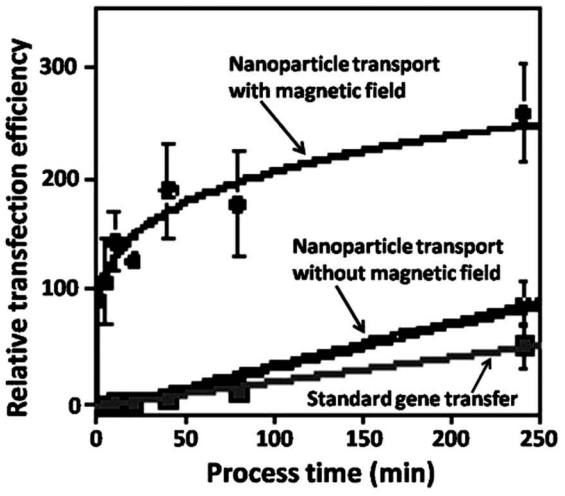

(b)

FIG. 4. Nanoparticle accumulation: (a) % of particles at the base of the chamber vs magnet-to-chamber spacing s, (b) measured relative transfection efficiency, with and without an applied field (adapted from [28]).

structure shown in Fig. 1(b). We solve for both the radial and axial force components,

$$\mathbf{F}_m(r,z) = F_{mr}(r,z)\hat{\mathbf{r}} + F_{mz}(r,z)\hat{\mathbf{z}}, \tag{A1}$$

where

$$F_{mr}(r,z) = \mu_0 V_p f(H_a)\left(H_{ar}(r,z)\frac{\partial H_{ar}(r,z)}{\partial r} + H_{az}(r,z)\frac{\partial H_{ar}(r,z)}{\partial z}\right), \tag{A2}$$

$$F_{mz}(r,z) = \mu_0 V_p f(H_a)\left(H_{ar}(r,z)\frac{\partial H_{az}(r,z)}{\partial r} + H_{az}(r,z)\frac{\partial H_{az}(r,z)}{\partial z}\right), \tag{A3}$$

and

$$\mathbf{H}_a = H_{ar}(r,z)\hat{\mathbf{r}} + H_{az}(r,z)\hat{\mathbf{z}}. \tag{A4}$$

In order to determine the force, we need an expression for the field distribution. To this end, we treat the magnet as an equivalent current source (see Sec. 3.3 of [29]; additional models for permanent magnet structures can be found in [30–34]. A cylindrical magnet that is uniformly magnetized along its axis produces the same field as a sheet of current that circulates around its circumference. We obtain the field distribution above the magnet by decomposing the "equivalent" current sheet into infinitesimal current loop elements and integrating the field contributions from the individual elements. The 2D field solution for a current loop is well-known (see p. 263 in [35]). If the magnet is magnetized to saturation M_s, and centered about the z axis with its top surface at $z=0$ as shown in Fig. 1(b), the applied field is given by

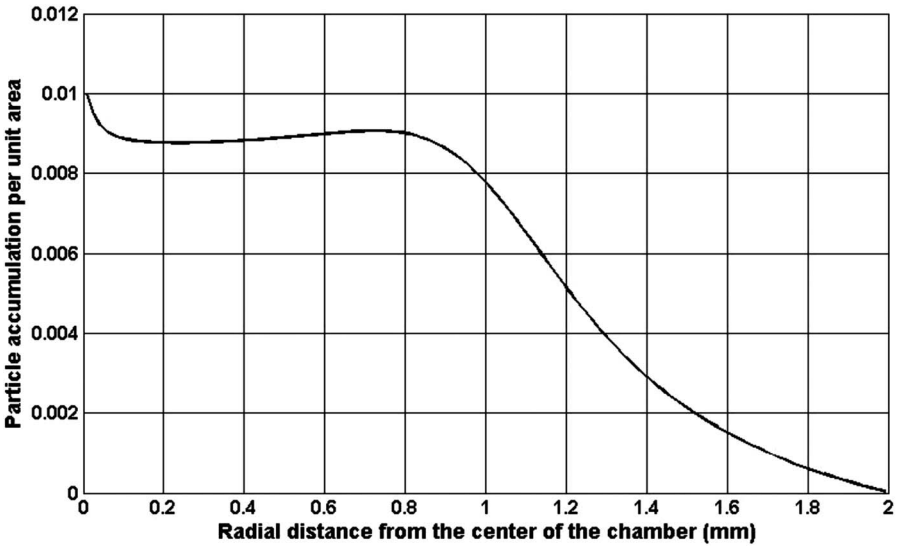

FIG. 5. Distribution of particle accumulation per unit area at the base of the chamber.

$$H_{ar}(r,z) = \frac{M_s}{2\pi}\int_{-L_m}^{0} \Pi_r(r,z)dz,$$

$$H_{az}(r,z) = \frac{M_s}{2\pi}\int_{-L_m}^{0} \Pi_z(r,z)dz, \tag{A5}$$

where

$$\Pi_r(r,z) = \frac{z}{r[(R_m+r)^2+z^2]^{1/2}}\left(\frac{(R_m^2+r^2+z^2)}{[(R_m-r)^2+z^2]}E(k) - K(k)\right), \tag{A6}$$

and

$$\Pi_z(r,z) = \frac{1}{r[(R_m+r)^2+z^2]^{1/2}}\left(\frac{(R_m^2-r^2+z^2)}{[(R_m-r)^2+z^2]}E(k) + K(k)\right). \tag{A7}$$

In these expressions, $K(k)$ and $E(k)$ are the complete elliptic integrals of the first and second kind, respectively [36],

$$K(k) = \int_0^{\pi/2} \frac{1}{\sqrt{1-k^2\sin^2(\phi)}}d\phi,$$

$$E(k) = \int_0^{\pi/2} \sqrt{1-k^2\sin^2(\phi)}d\phi, \tag{A8}$$

where

$$k^2 = \frac{4rR_m}{(R_m+r)^2+z^2}. \tag{A9}$$

From Eqs. (A6) and (A7), we find that

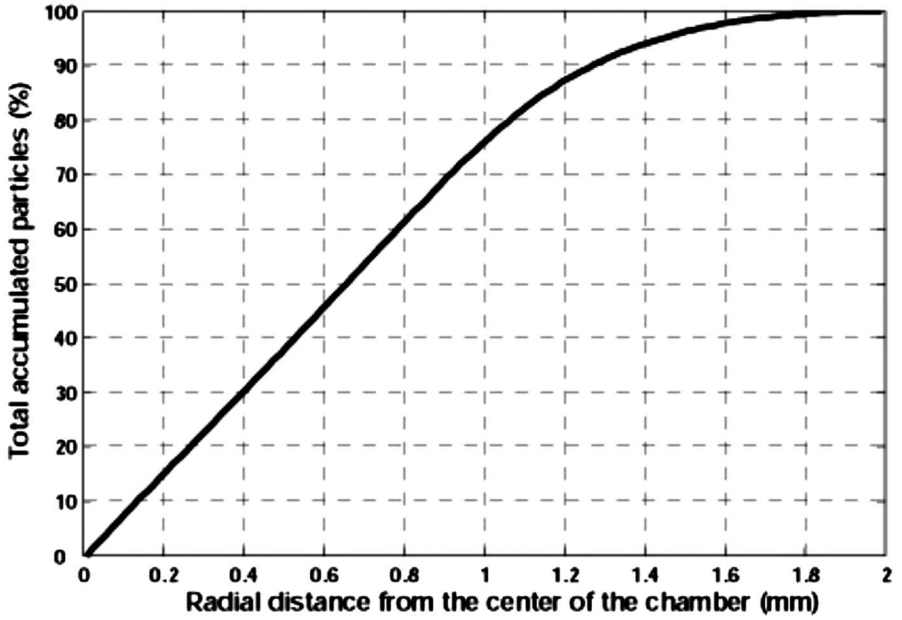

FIG. 6. Normalized total particle accumulation at the base of the fluidic chamber as a function of the radial distance from its center.

$$\frac{\partial \Pi_r(r,z)}{\partial r} = \frac{f^2}{rd}\left([(R_m^2+z^2)^2 + r^2(-3R_m^2+2r^2+3z^2)]\Pi_r + \frac{6R_m^2 rz(R_m^2-r^2+z^2)f}{d}E(k)\right), \quad \text{(A10)}$$

$$\frac{\partial \Pi_r(r,z)}{\partial z} = \frac{\partial \Pi_z(r,z)}{\partial r} = \frac{-f^2}{zd}\left([z^2(R_m^2+r^2) + (R_m^2-r^2)^2]\Pi_r + \frac{12R_m^2 rz^3 f}{d}E(k)\right), \quad \text{(A11)}$$

and

$$\frac{\partial \Pi_z(r,z)}{\partial z} = \frac{zf^2}{d}\left((R_m^2-r^2-z^2)\Pi_z - \frac{4R_m^2(2R_m^2-2r^2+z^2)^2 f}{d}E(k)\right), \quad \text{(A12)}$$

where

$$d = (R_m - r)^2 + z^2 \quad \text{and} \quad f = \frac{1}{[(R_m+r)^2+z^2]^{1/2}}. \quad \text{(A13)}$$

We substitute Eqs. (A5)–(A13) into Eqs. (A2) and (A3) to evaluate the 2D magnetic force.

[1] F. Marcucci and F. Lefoulon, Drug Discovery Today **9**, 219 (2004).
[2] Q. A. Pankhurst, J. Connolly, S. K. Jones, and J. Dobson, J. Phys. D **36**, R167 (2003).
[3] *Scientific and Clinical Applications of Magnetic Carriers*, edited by U. Hafeli, W. Schutt, and J. Teller (Plenum, New York, 1997).
[4] C. C. Berry and A. S. G. Curtis, J. Phys. D **36**, R198 (2003).
[5] A. Ito, M. Shinkai, H. Honda, and T. Kobayashi, J. Biosci. Bioeng. **100**, 1 (2005).
[6] U. Schillinger, T. Brilla, C. Rudolph, S. Huth, S. Gersting, F. Krötz, J. Hirschberger, C. Bergemann, and C. Plank, J. Magn. Magn. Mater. **293**, 501 (2005).
[7] C. Plank, U. Schillinger, F. Scherer, C. Bergemann, J.-S. Rémy, F. Krötz, M. Anton, J. Lausier, and J. Rosenecker, Biol. Chem. **384**, 737 (2003).
[8] F. Scherer, M. Anton, U. Schillinger, J. Henke, C. Bergemann, A. Kruger, B. Gansbacher, and C. Plank, Gene Ther. **9**, 102 (2002).
[9] C. Plank, M. Anton, C. Rudolph, J. Rosenecker, and F. Krötz, Expert Opin. Biol. Ther. **3**, 745 (2003).
[10] C. Plank, F. Scherer, U. Schillinger, C. Bergemann, and M. Anton, J. Liposome Res. **13**, 29 (2003).
[11] C. Plank, F. Scherer, U. Schillinger, and M. Anton, J. Gene Med. **2**, Suppl., S24 (2000).
[12] C. Plank, J. Liposome Res. **13**, 29 (2003).
[13] J. Dobson, Gene Ther. **13**, 283 (2006).
[14] F. Krötz, C. Wit, H. Y. Son, S. Zahler, T. Gloe, U. Pohl, and C. Plank, Mol. Ther. **7**, 700 (2003).
[15] E. P. Furlani, J. Appl. Phys. **99**, 024912 (2006).
[16] R. Gerber, IEEE Trans. Magn. **20**, 1159 (1984).
[17] D. R. Kelland, IEEE Trans. Magn. **34**, 2123 (1998).
[18] D. Fletcher, IEEE Trans. Magn. **27**, 3655 (1991).
[19] L. P. Davies and R. Gerber, IEEE Trans. Magn. **26**, 1867 (1990).
[20] R. Gerber and R. R. Birss, *High Gradient Magnetic Separation* (Wiley, Somerset, NJ, 1983).
[21] R. Gerber, M. Takayasu, and F. J. Friedlander, IEEE Trans. Magn. **19**, 2115 (1983).
[22] M. Takayasu, R. Gerber, and F. J. Friedlander, IEEE Trans. Magn. **19**, 2112 (1983).
[23] E. P. Furlani and K. C. Ng, Phys. Rev. E **73**, 061919 (2006).
[24] T. P. Jones, *Electromechanics of Particles* (Cambridge University Press, Cambridge, UK, 1995).
[25] E. P. Furlani and Y. Sahoo, J. Phys. D **39**, 1724 (2006).
[26] E. J. Furlani and E. P. Furlani, J. Magn. Magn. Mater. **312**, 187 (2007).
[27] E. P. Furlani, Y. Sahoo, K. C. Ng, J. C. Wortman, and T. E. Monk, Biomed. Microdevices **9**, 451 (2007).
[28] C. Plank, F. Scherer, U. Schillinger, M. Anton, and C. Bergemann, Eur. Cells Mater. **3** (Suppl. 2), 79 (2002).
[29] E. P. Furlani, *Permanent Magnet and Electromechanical Devices; Materials, Analysis and Applications* (Academic, New York, 2001).
[30] E. P. Furlani, IEEE Trans. Magn. **33**, 2317 (1997).
[31] E. P. Furlani, J. Appl. Phys. **79**, 4692 (1996).
[32] E. P. Furlani, IEEE Trans. Magn. **31**, 844 (1995).
[33] E. P. Furlani, IEEE Trans. Magn. **30**, 3660 (1994).
[34] E. P. Furlani, J. Magn. Magn. Mater. **135**, 205 (1994).
[35] J. A. Stratton, *Electromagnetic Theory* (McGraw-Hill, New York, 1941).
[36] G. Arfken, *Mathematical Methods for Physicists*, 3rd ed. (Academic, New York, 1985).